DOI: 10.1002/cphc.201200069

Photoanodes Based on Nanostructured WO_3 for Water Splitting

Alessandra Tacca,*[a] Laura Meda,[a] Gianluigi Marra,[a] Alberto Savoini,[a] Stefano Caramori,*[b] Vito Cristino,[b] Carlo Alberto Bignozzi,[b] Victoria Gonzalez Pedro,[c] Pablo P. Boix,[c] Sixto Gimenez,[c] and Juan Bisquert[c]

Anodically grown WO_3 photoelectrodes prepared in an *N*-methylformamide (NMF) electrolyte have been investigated with the aim of exploring the effects induced by anodization time and water concentration in the electrochemical bath on the properties of the resulting photoanodes. An n-type WO_3 semiconductor is one of the most promising photoanodes for hydrogen production from water splitting and the electrochemical anodization of tungsten allows very good photoelectrodes, which are characterized by a low charge-transfer resistance and an increased spectral response in the visible region, to be obtained. These photoanodes were investigated by a combination of steady state and transient photoelectrochemical techniques and a correlation between photocurrent produced, morphology, and charge transport has been evaluated.

1. Introduction

Photoelectrochemical water splitting, that is, the decomposition of water into elemental hydrogen and oxygen by exploiting solar energy and semiconductor photoelectrodes, is an attractive field of research due to the possibility of absorbing and converting sunlight into high-energy charge carriers that can drive water oxidation and reduction reactions in the separate compartments of a photoelectrochemical cell (PEC) with high quantum yields. This process may allow for the production of virtually inexhaustible renewable fuel, if reasonably high efficiencies are achieved. To be economically viable, the current estimates require a solar power to hydrogen conversion efficiency in the order of 10%. While this objective is still far from being achieved by using cheap, easy to manufacture, and stable materials, the development of PECs has generally gained considerable benefits by the development of nanostructured materials based on n-type metal oxides, such as TiO_2,[1] Fe_2O_3,[2] and WO_3;[3] these have attracted most attention due to their low cost, ease of preparation, and high stability in aqueous solution under oxygen-evolving conditions. More recently, metal oxynitrides, such as TaON,[4] or phosphates, such as Ag_3PO_4,[5] have shown very promising photoanodic responses, although their preparation and stability under prolonged illumination seems to be more critical than for simpler metal oxides.

Among these, tungsten oxides have unique properties, such as chromism, sensing capabilities,[6] and very good surface stability. Efforts to increase efficiency by controlling the nanostructure of the photoanodes have been conducted to maximize the contact area between the electrode and electrolyte and to optimize the electron-transport pathways.[7] To obtain an extended electrochemically active surface, effective light harvesting, and reasonably good charge transport and collection efficiencies, different synthetic routes are employed for nanocrystalline WO_3. Template-mediated synthesis, hydrothermal, wet organic and inorganic routes, and thermal methods have been reported.[6,8]

Sol–gel methods developed by Augustynski et al.[3] allow highly transparent nanoporous WO_3 films to be obtained that can be characterized by photocurrent versus excitation wavelength spectra exhibiting maxima close to 400 nm.[9]

The electrochemical anodization of metals such as titanium or tungsten is an alternative preparative route, which can lead to the growth of interesting crystalline oxide nanostructures directly bound to the metal collector, thus providing the basis for efficient charge collection.[10–11] The comparatively high metal conductivity also allows for the production of large-area photoanodes that do not suffer from ohmic limitations typical of transparent-conducting oxide (TCO) collectors.[12] In particular, anodization in *N*-methylformamide (NMF)-based electrolytes led to very good photoanodes, characterized by a low charge-transfer resistance and an increased spectral response in the visible region, in agreement with an experimentally de-

[a] *Dr. A. Tacca, Dr. L. Meda, Dr. G. Marra, Dr. A. Savoini*
Istituto ENI Donegani
Via Fauser 4, 28100, Novara (Italy)
Fax: (+39) 0321447425
E-mail: alessandra.tacca@eni.com

[b] *Dr. S. Caramori, Dr. V. Cristino, Prof. C. A. Bignozzi*
Department of Chemistry, Ferrara University
Via Luigi Borsari 46, 44121 Ferrara (Italy)
Fax: (+39) 0532 240709
E-mail: cte@unife.it

[c] *Dr. V. G. Pedro, Dr. P. P. Boix, Dr. S. Gimenez, Prof. J. Bisquert*
Department of Physics, Universitat Jaume I
12071, Castello (Spain)

Supporting information for this article is available on the WWW under http://dx.doi.org/10.1002/cphc.201200069.

termined indirect optical band gap of 2.66 eV.[14a–c] The electrochemical formation of a porous metal oxide can be understood in terms of at least two competing interfacial processes: oxide formation by reaction with oxygen donors, commonly water, resulting in the initial formation of a compact oxide layer and the field-assisted dissolution of the oxide coupled with chemical etching by fluorides.[14b,d,e] Clearly, the characteristics of the outer oxide layer, with regard to a specific electroactive surface, electrolyte permeation, charge transport, and interfacial charge-transfer dynamics are of crucial importance for optimizing current generation by the photoanode. Efforts should still be undertaken to find the best anodizing conditions (solvent composition, temperature, potential/current program) to obtain a photoactive surface that maximizes the photocurrent output and subsequent solar power to hydrogen conversion. In this context, we explore the effects induced by anodization time and water content in the electrolytic bath on the morphology and performance of a series of anodically grown WO_3 photoanodes prepared in an NMF-based electrolyte. These photoelectrodes were characterized by a combination of structural, steady state, and transient photoelectrochemical techniques with the aim of rationalizing the main factors at the basis of an efficient photoanodic response.

2. Results and Discussion

2.1. Morphology

WO_3 anodization process at room temperature in the presence of 20% water was described in recent works.[14] To shorten the anodization time, the process temperature was increased to 40 °C .[14c] The typical oscillating shape of the anodization current is reported in Figure S1 in the Supporting Information and an exchanged charge value of 1200 $C\,cm^{-2}$ is obtained after only 6 h of anodization[14b] instead of 72 h. As a matter of fact, the resulting tungsten oxide presents a peculiar "crispy" shape, which is composed of nanoparticles with an average diameter of 50–70 nm (Figure 1) interconnected by a nanoscopic structure with an average layer thickness of about 2.18 μm (Figure 2).

The formation of this new nanostructure is mainly attributed to competition between oxide formation and fluoride-induced and electrical-field-assisted etching. After anodization for a few minutes, when a very low current intensity is recorded, a compact oxide layer is formed and only a few corrosion pits are present on the surface. After 1 h, the number of pits grows rapidly when the exchanged current reaches a maximum and etching of the oxide layer is the predominant phenomenon. The following current decrease and stabilization are due to oxide consolidation in 2–3.5 h, that is, an increased thickness of the wall pores (Figure 3). In 5–6 h the crispy morphology is complete, showing strong similarities with that observed at the end of room-temperature processing,[14c] indicating that the improved interfacial kinetics observed at 40 °C may be conveniently exploited for a relatively fast photoelectrode production.

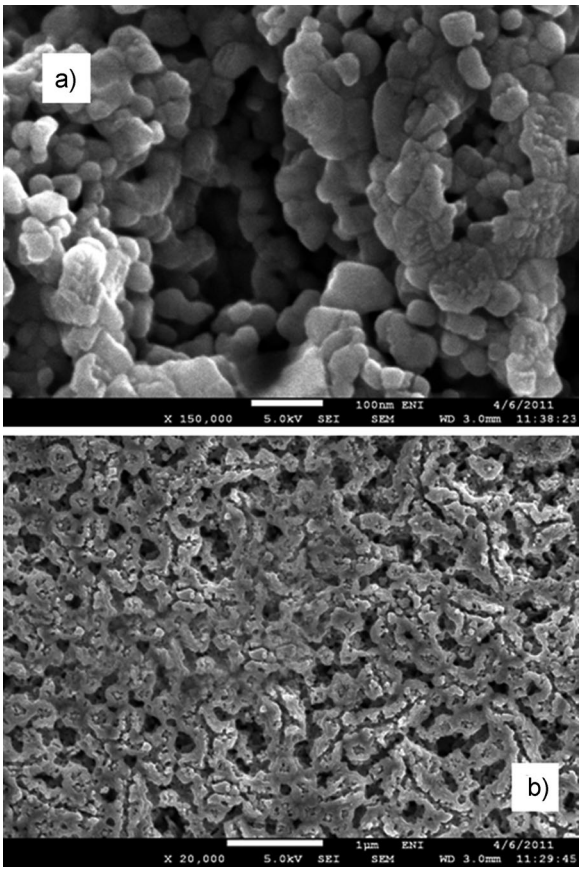

Figure 1. SEM micrographs of the surface of anodic growth in WO_3 (20, 6 h) at a magnification of 150 000× (a; scale bar 100 nm) and 20 000× (b; scale bar 1 μm).

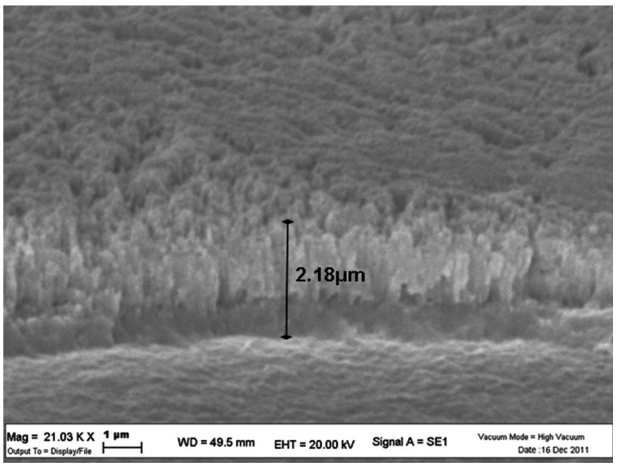

Figure 2. SEM micrograph (21 000 000×) of a cross-section of anodized WO_3 (20, 6 h). Scale bar 1 μm.

The heterogeneous distribution of particles and their organization in larger nanostructures are difficult to tune and control with this kind of synthesis, which is strictly dependent on the reactants and experimental parameters, for example, temperature, the distance between electrodes, and the water and fluoride content in the electrolytic bath during anodization. Small

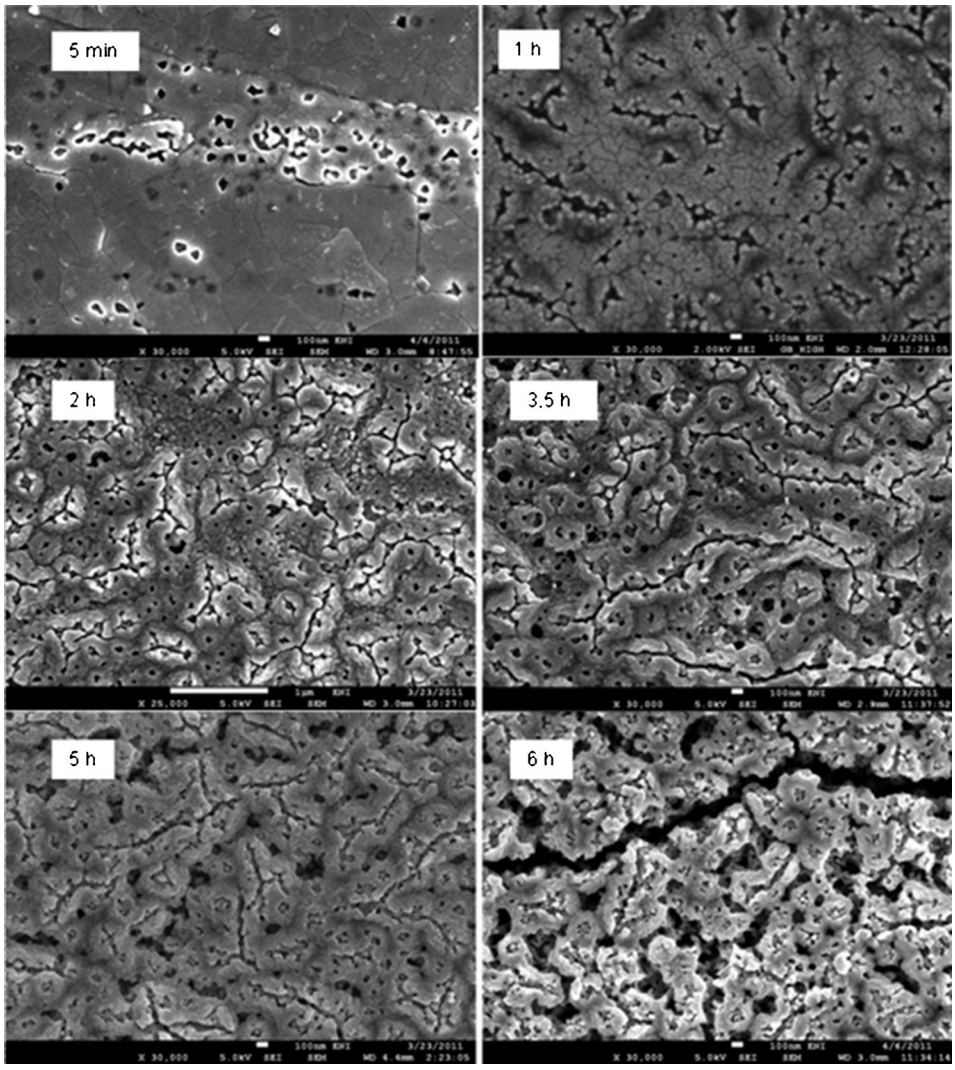

Figure 3. SEM micrographs of surfaces of the anodic growth of WO_3 at increasing anodization time from 5 min to 6 h. Scale bars: 100 nm for 5 min, 1 h, 3.5 h, 5 h, and 6 h; 1 μm for 2 h.

perturbations could lead to totally different morphologies with different performances. In particular, the effect of the amount of water seems to be an influential parameter and was used as a case of study. The concentration of water in the NMF-based electrolyte was systematically varied from 10 to 50% v/v to investigate its effect on the performances of the resulting photoelectrodes.

The SEM micrographs of electrode 10 (Figure 4a) show the same morphology of the previous one (Figure 1); however, the columnar structures visible in the cross-section are not so clear or well separated, even if electrode 10 (named for the water content) exhibits relatively compact oxide walls about 2 μm high. In sample 30 the characteristic crispy surface crust is lost and replaced by a homogenous coverage of small, interconnected needle-like particles, which resembles the structure of a sponge (Figure 4b). The cross-sectional view reveals that these surface features are simply irregular edges of underlying vertically oriented columnar structures 2 μm high (Figure 4b). When the amount of water in the anodization bath increases then the surface of the photoanode becomes more compact and the oxide layer also becomes thinner. The surface of sample 40 shows irregular features with nanostructure edges similar to those of sample 30 (Figure 4c). The thicknesses of samples 40 and 50 are also similar and about half of that observed in 10, 20, and 30 (Figure 4). In both cases the cross-sectional views suggest the presence of a closely packed oxide layer, which may limit the permeation of the electrolyte into the inner layers. Sample 40 is thinner (0.75 μm) than 50 (ca. 1.1 μm); however, the oxide structure in sample 50 seems to be less porous, the surface has only shallow corrosion pits and channels (Figure 4). The relatively low stationary current of 10 mA, associated with the anodization of sample 50, suggests that the increased amount of water shifts the equilibrium between oxide formation and dissolution by favoring the formation of a compact oxide layer acting as an insulating barrier. This is expected from the relevant concentration of oxygen donors present in this type of electrolyte formulation.

In contrast, the higher, slowly decreasing currents observed with samples 20 (Figure S1 in the Supporting Information) and 30 suggest a set in of conditions in which the continuous formation of new fresh oxide at the metal/oxide interface follows field-assisted dissolution, resulting in a progressive inward movement of the interface and in the formation of the porous oxide network evidenced in Figure 3.

In all cases the diffraction pattern of anodized WO_3 films indicates the presence of a crystalline monoclinic phase (Figure S2 in the Supporting Information). It is worthwhile noting that the XRD pattern of the anodically grown samples is consistent with a preferential orientation of the 020 and 222 crystal planes. Consequently, the 040 and 060 signals become evident. Moreover, anisotropy along 222 increases proportionally with the anodization time, as shown in Figure S3 in the Supporting Information. No orientation is present after 1 h; this is reasonable because under these conditions only pits are present on the oxide surface. Aggregation and wall formation, which lead to the crispy nanostructure, begin after at least two hours of the electrochemical reaction. Preferential growth was

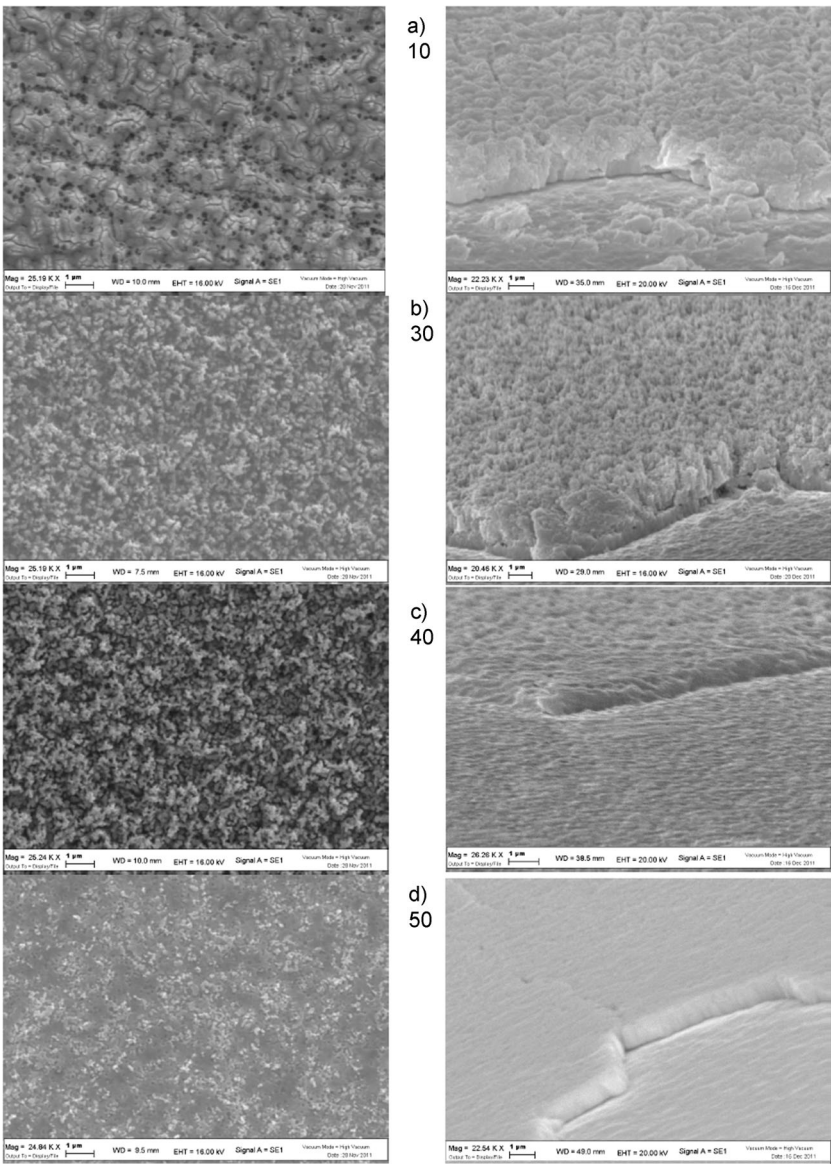

Figure 4. SEM micrographs of the surface (left) and cross-section (right) of anodic growth of WO_3 at increasing water contents of 10 (a), 30 (b), 40 (c), and 50% (d). Scale bars 1 μm.

already described by Guo et al. for WO_3 samples obtained by anodization in an aqueous acidic bath; however, those structures were not characterized by a similar morphology.[15]

The same type of preferential orientation is also present in samples anodized with different water contents. In Figure S4 in the Supporting Information the XRD peak decreases with the trend for samples $30 > 40 > 10$.

The 50% sample does not show any anisotropy and has a morphological similarity to electrodes obtained at early anodization times (5 min to 1 h) in 20% water in which a compact oxide layer was observed.

AFM imaging gives a topographical picture of the surface and confirmed the nanostructured morphology seen in the SEM micrographs (Figure 5 and Figures S5 and S6 in the Supporting Information). Moreover, this technique can provide a relative evaluation of the surface area. This method is based on imaging analysis and it provides a value normalized to the evaluated area. In Figure 6 the calculated values were plotted as a function of the anodization time: the surface area slowly increases to reach a maximum after 6 h and then decreases.

The maximum height difference between structure crests and valleys or pores does not significantly change in from 2 to 7 h of anodization and is approximately 550 nm.

2.2. Photoelectrochemistry

Electrochemical tests were performed to evaluate the ability of WO_3 as a photoanode in a photoelectrochemical cell.

Figure 7a shows the *J–V* characteristics recorded in 1 M H_2SO_4 under full xenon illumination at 0.3 W cm^{-2} for samples anodized at increasing times in the presence of 20% water. The performance of the 6 h sample is superior to all the other electrodes: it reaches 3.8 mA cm^{-2} at 1 V versus SCE and 4.8 mA cm^{-2} at 1.5 V versus SCE. The open-circuit potential is 0.25 V versus SCE for all samples: different anodization times do not affect this value. These performances confirmed that, even from a photoelectrochemical point of view, the accelerated anodization route for 6 h leads to WO_3 samples comparable to those obtained from long room-temperature processes.[14]

As shown in Figure 7b, the photoanodic current increased with the process time, until a maximum value was observed for the 6 h sample, and then decreased again for the 7 h sample. This behavior is probably determined by the amount of electroactive surface of each sample, since the observed trend qualitatively parallels the relative variations in the specific surface area estimated by AFM measurements, although only the outermost oxide layers (ca. 1/4 of the total WO_3 thickness in the thickest samples) are available to this technique. The highest currents are indeed expected in those electrodes that display the highest electroactive area, enabling more efficient hole transfer to the electrolyte.

The photoaction spectra [incident photon to current efficiency (IPCE) vs. wavelength] corroborate the observations drawn from the *J–V* characteristics (Figure 8): the spectra recorded in

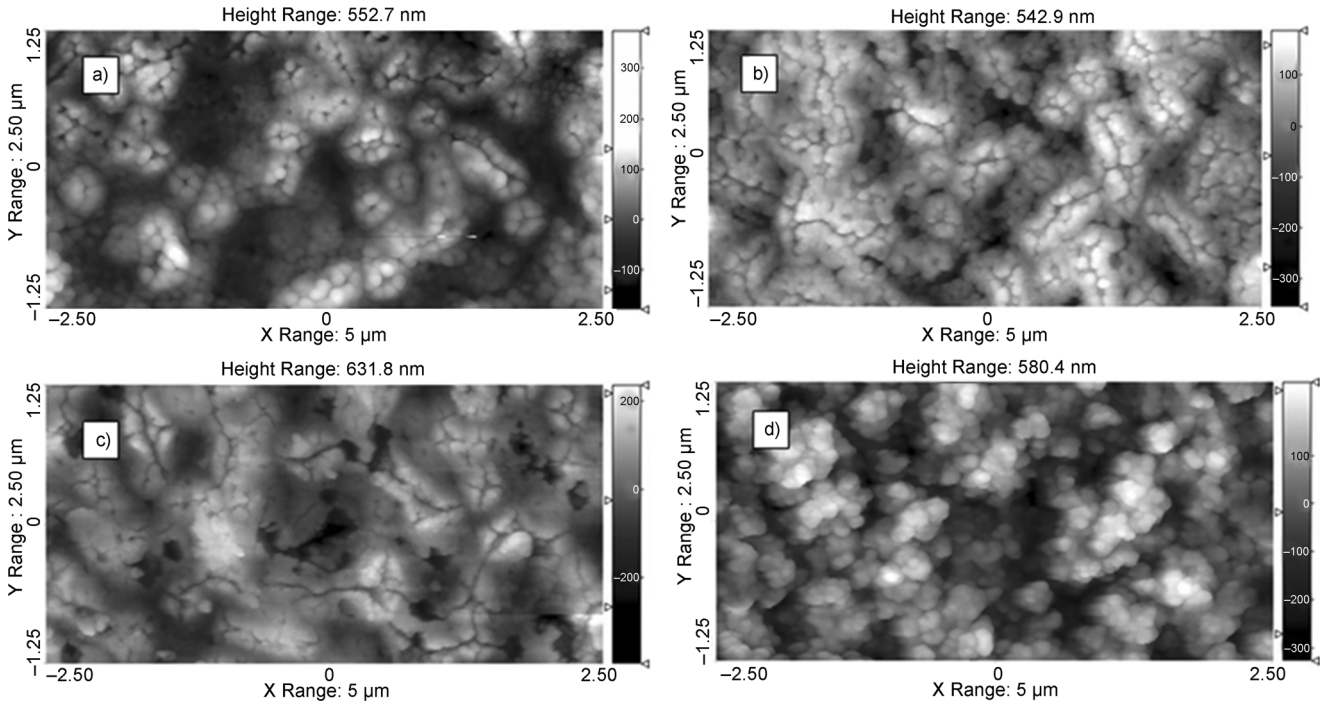

Figure 5. AFM images of WO_3 anodized for 2 (a) and 6 h (b) with 10 (c) and 40% (d) water.

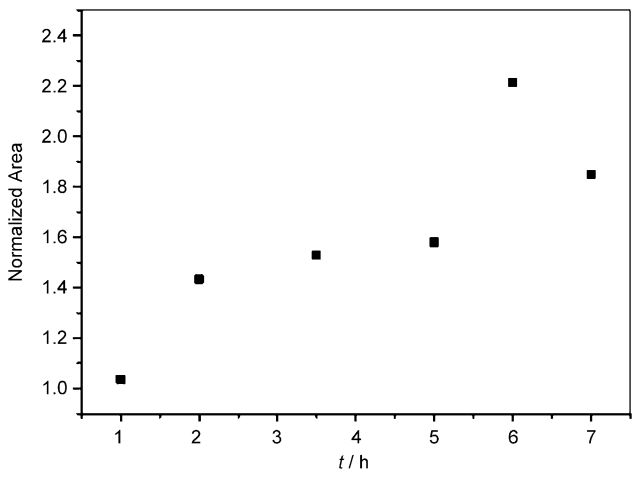

Figure 6. Normalized area of the anodized WO_3, elaborated from AFM images, as a function of anodization time.

sulfuric acid, at 1.5 V versus SCE, indicate the highest photon-to-current conversion in samples anodized for 6 and 5 h, approaching 70% in the UV region, extending deeply into the visible region with a secondary shoulder at 400 nm, the onset of which is located at 480 nm. As expected, the sample anodized for 1 h shows the worst performance with a maximum conversion efficiency lower than 30% and a negligible response to visible wavelengths.

The 6 h sample was also investigated under a variable illumination intensity: the incident irradiance was varied from 10 to 300 mW cm^{-2} to simulate the performance of the cell in an

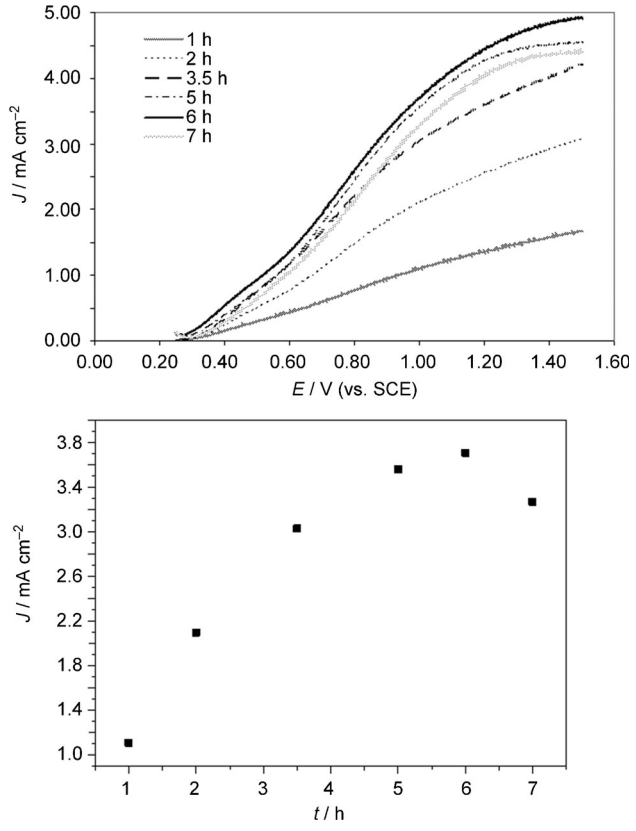

Figure 7. a) Typical *J*–*V* curves obtained in 1 M H_2SO_4 under illumination at 0.3 W cm^{-2} with a full xenon lamp in a three-electrode configuration for samples obtained at increasing anodization times. b) Trend of *J* values at 1 V versus a saturated calomel electrode (SCE) as a function of anodization time.

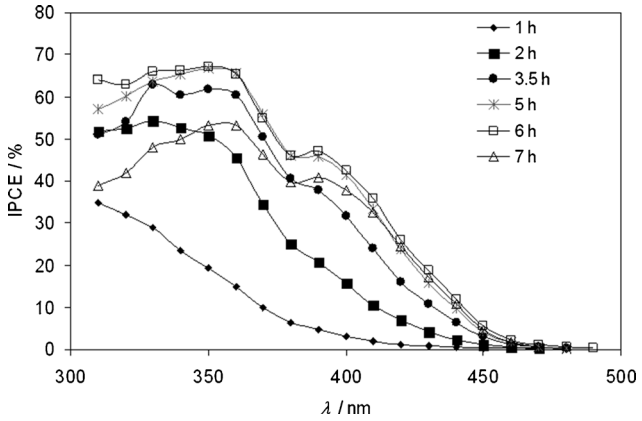

Figure 8. IPCE spectra of WO_3 anodized at increasing times under a 1.5 V versus SCE potential bias.

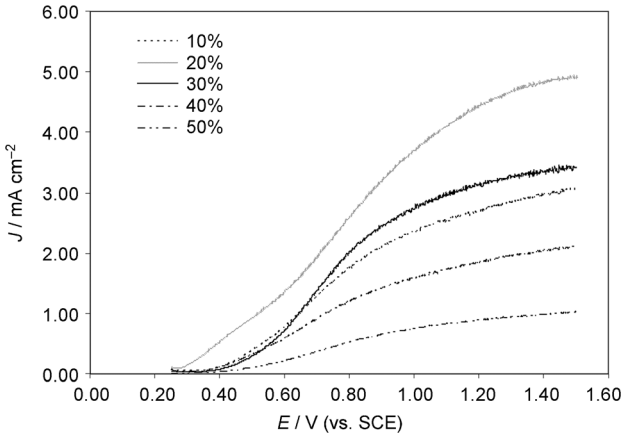

Figure 10. *J–V* curves of the samples with 10–50% water content obtained in 1 M H_2SO_4 under illumination at 0.3 W cm^{-2} with a full xenon lamp.

outdoor system in the dark, on a cloudy day, and in the presence of a solar concentrator. The two-electrode configuration was chosen to evaluate the performance of the whole cell.[16]

As shown in Figure 9, the photocurrent response grows almost linearly with an illumination power of up to 300 mW cm^{-2} and it does not show any saturation under high

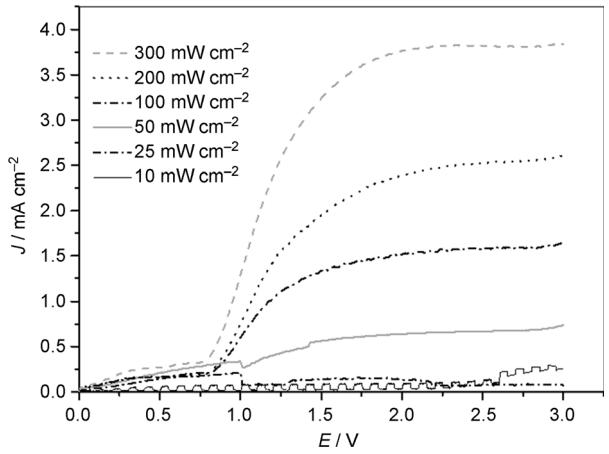

Figure 9. *J–V* characteristics in two-electrode configuration at increasing incident irradiance for WO_3 anodized for 6 h.

power intensities, indicating a very effective hole transfer to the electrolyte.

Figure 10 shows the *J–V* characteristics recorded in 1 M H_2SO_4 under simulated 0.3 W cm^{-2} AM 1.5 illumination for samples anodized in the presence of a variable water content (10–50%).

As expected, the anodization conditions strongly affect the photoelectrochemical response of the resulting photoanodes, which display marked variations within the series: the sample with 20% water is by far the best photoelectrode, with a maximum photocurrent close to 5 mA cm^{-2}, followed by samples 10 and 30, which exhibit similar performances with a maximum *J* approaching 3 mA cm^{-2}. The worst performance is observed with the thinnest electrodes (samples 40 and 50), with *J* lower than 2 mA cm^{-2}. The best conversion efficiencies were, however, still low and in the order of 0.15% under an applied bias of 1 V in a two-electrode configuration. This is mainly due to the need for a strong positive bias to achieve a relevant photocurrent, indicating that WO_3 electrodes always require an external voltage source, which may be provided by a photovoltaic cell or a p-type cathode, to operate with reasonable efficiency. In fact, optimization of the whole final cell has not yet been performed.

IPCE spectra confirm the observed trend, indicating broad and reasonably high photoconversion (ca. 50%) for samples 10 and 30, which display an onset at 470 nm. Sample 20 shows the best performance in the visible region (Figure 11), also thanks to improved light absorption due to increased light

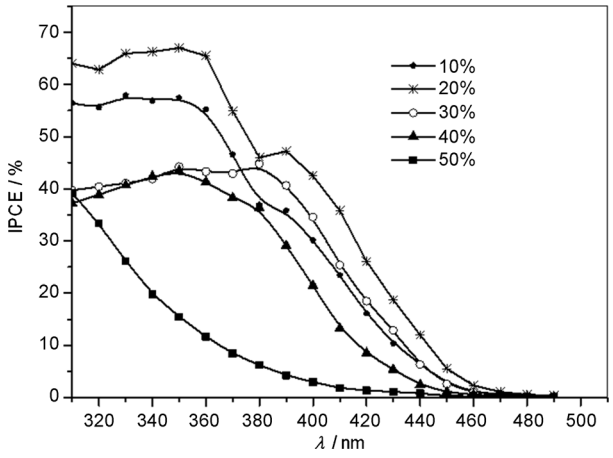

Figure 11. IPCE spectra of the samples with 10–50% water content under a 1.5 V versus SCE potential bias.

scattering induced by the irregular nanostructures, as suggested by the sharp decrease in reflected light evidenced by the diffuse reflectance (DR) spectra reported in Figure S13 in the Supporting Information. Thus, the vertically oriented, porous structures encountered in electrodes for samples 10, 20, and

30 are suitable for improving light harvesting and to achieve good electrolyte permeation of the oxide substrate as well as a short hole diffusion path, as demonstrated by the good conversion for those wavelengths with a long penetration depth in the semiconductor (i.e. $\approx$7 μm at 440 nm)[17] and create an electron–hole pair far from the outermost layer of the oxide. In contrast, more compact oxide layers, such as those observed in electrodes for the 1 h sample or that with 50% water, only display a reasonable conversion in the UV region (300–360 nm) in which the radiation has a short penetration depth (ca. 1 μm)[17] and generates electron–hole pairs in the outermost oxide layers, which have a better chance of being more effectively permeated by the electrolyte. This seems to contradict the common notion that, if the charge carriers are generated in close proximity to the electron collector then are efficiently extracted; however, if the inner part of the oxide is barely accessible to the electrolyte, hole transfer to the latter cannot be efficiently achieved and electron/hole recombination occurs on the millisecond timescale, as revealed by the fast component of laser-induced photovoltage decay measurements (Figure S11 and S12 in the Supporting Information).

The impedance characteristics of the electrodes could be well fitted by the circuit shown in Scheme 1 (Figures S7 and S9 in the Supporting Information). In all cases, the impedance of

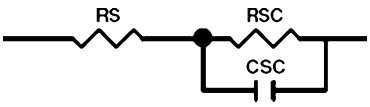

Scheme 1. Equivalent circuits employed for fitting of the EIS data. *Rs* represents the ohmic resistance of the solution and of the electric contacts, *Rsc* is a charge-transfer resistance (*R*ct), and CSC is the nonideal capacitance of the space charge layer described by a constant phase element (CPE).

the photoelectrodes is dominated by the charge-transfer resistance (*R*ct) which is usually in the range of 102–103 Ω, with only a negligible contribution (ca. 1 Ω) arising from the ohmic resistances (electrolyte and wires) of the cell, given the high conductivity of the 1 M sulfuric acid solution. No electron-transport impedance features were observed in the high-frequency region for any of the electrodes at any of the explored potentials and we have to assume negligible electron transport resistance, which is in agreement with the relatively fast electron transport observed in transient experiments (see below). A detailed investigation into the transmission line in anodic WO_3 electrodes is currently underway in collaboration with the group of Bisquert and the preliminary results confirm such observations. The charge-transfer resistance uniquely determines the shape and the size of the *J–V* curves, as seen by the good agreement between the reciprocal of the charge-transfer resistance and the derivative of the *J–V* curve (Figure S8 in the Supporting Information). The lowest charge-transfer resistance is indeed observed in the case of sample 20. To elucidate the origin of the marked improvement in performance by controlling the amount of water in the anodization solution, electrochemical impedance spectroscopy (EIS) analysis of the modified photoanodes was carried out. The impedance was measured at applied potentials from 0.2 to 1.2 V versus SCE, which coincides with the potential region where the photocurrent rises. We aimed to obtain EIS data under conditions where the semiconductor generated photocurrent and to correlate the impedance response directly to the physical processes responsible for the photocurrent, not to passive circuit elements. Consequently, results for anodically grown (20 and 50% water) and colloidal nanoporous electrodes 0.8 μm thick previously described by Meda et al. were compared.[9]

The results obtained clearly showed space charge effects for the anodically grown electrodes, as a result of the presence of a barrier layer.[18] In contrast, colloidal electrodes do not reveal any evidence of space charge effects, showing behavior closer to chemical capacitance,[19] although this hypothesis needs to be confirmed with more accurate investigations. The Mott Schottky (M-S) plots (C^{-2} vs. V) corresponding to the space charge capacitance of the WO_3 layer formed in the 20 and 50% H_2O specimens are shown in Figure S10 in the Supporting Information. Similar results were obtained for both structures (20 and 50% H_2O) after normalizing with the corresponding active area (values obtained from AFM). The M-S plots correspond to an n-type semiconductor, and from this representation, both the donor density (N_D) at the space charge region and the flat band potential (E_{fb}) can be estimated. The values obtained for E_{fb} were approximately 0.24–0.25 V versus SCE and $1.50–1.85\times10^{20}$ cm^{-3} for N_D, similar to those previously reported for this material.[18,20–21] Indeed, for such a high doping level (10^{20} cm^{-3}), the depletion zone is around 5 nm, which justifies the similar values for both specimens. From these values, it can be concluded that the WO_3 film behaves as a compact layer and optimization of the water concentration in the anodization solution leads to effective surface pitting and higher WO_3/electrolyte interfacial area. The increased surface roughness facilitates penetration of the electrolyte, enhancing hole injection from WO_3 to the electrolyte and promoting charge separation. Furthermore, the higher irregularity of the film can reduce the bulk hole diffusion path, although this possibility still needs to be verified.

While the EIS measurements provided information about interfacial processes, to investigate the effect of different oxide morphologies on the electron transport, laser-induced photocurrent transient measurements were performed. The electrodes of samples 10–50 were tested in 1 M H_2SO_4 at 1 V versus SCE and their time-resolved photocurrent decays are reported in Figure 12a. Assuming a 355 nm absorption coefficient of about 3 10^6 M^{-1}, the vast majority of the incident photons (>90%) are absorbed within a WO_3 layer approximately 1 μm thick, leading to the almost complete absorption of the excitation light by all WO_3 samples under investigation. From Figure 12a we can appreciate that τ_p varies in the order $20>10>30>40>50$ (Table 1). In all cases charge transport is efficient, with a sub-millisecond photocurrent rise time and a total peak width of a few milliseconds. The apparent electron diffusion coefficients calculated according to $D=W^2/2\tau_{peak}$[22] are found to be set in a relatively narrow range between about 2.3×10^{-5} and 0.8×10^{-5} cm^2s^{-1} (Table 1). Qualitatively, thinner electrodes

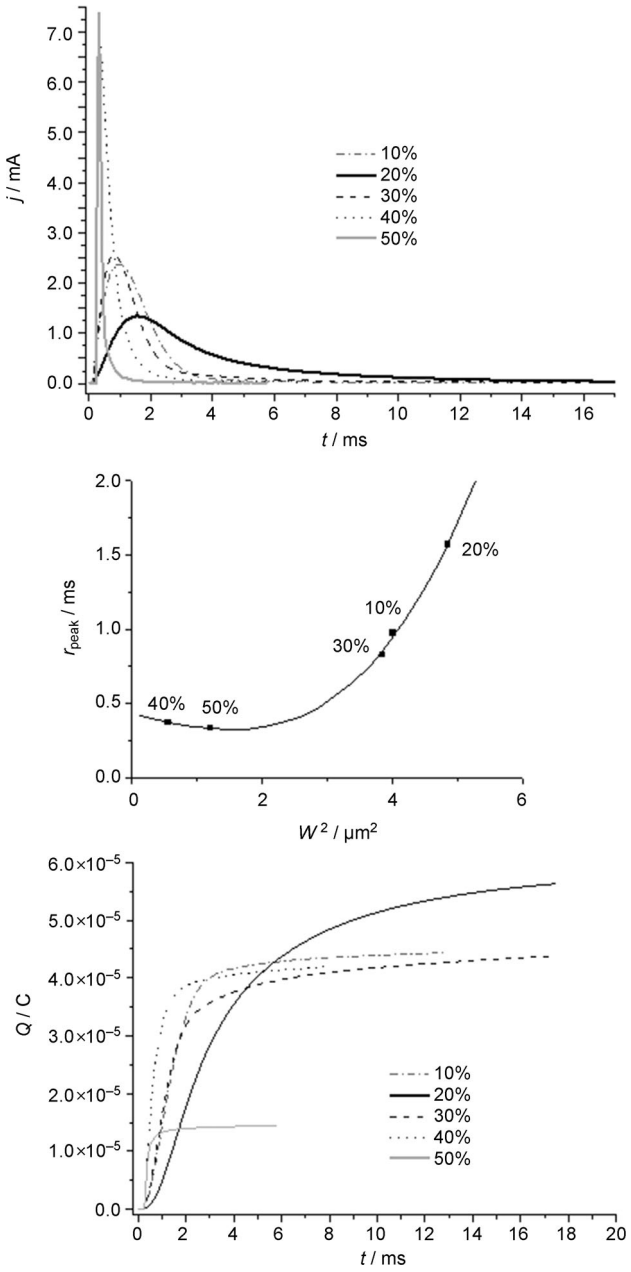

Figure 12. a) Laser-induced photocurrent transients (at 355 nm) at 1 V versus SCE; b) τ_{peak} versus W^2; c) extracted charge (Q) at 1 V versus SCE.

Table 1. Photocurrent peak time τ_p, apparent electron diffusion coefficient (D), and extracted photocharge data following 355 nm laser excitation of the series of WO_3 samples.

Electrolyte	W [µm]	τ_p [ms]	$D \times 10^{-5}$ [$cm^2 s^{-1}$]	Q [µC]
10	2	0.97	2	4.44
20	2.2	1.57	1.54	5.62
30	1.96	0.83	2.31	4.38
40	0.75	0.37	0.76	4.2
50	1.1	0.33	1.83	1.45

result in shorter peak times, but the behavior is strongly nonlinear because D is not strictly constant, as shown in Figure 12b. Here an arbitrary polynomial function is used to interpolate the experimental data (τ_p vs. W^2) providing graphical evidence of the observed trend. The extracted charge (Q) varies in the order $20 > 10 > 30 > 40 > 50$. In fact, samples 10, 30, and 40 exhibit very close Q values, centered around 4.2×10^{-6} C, while sample 20 is, in this context, significantly better than the others (ca. 35%), probably due to improved hole scavenging. In addition, the photoinduced charge collected from sample 50 is much lower than that recorded in the case of sample 40, although the oxide thickness of the former is slightly higher than that of the latter. Since the amount of 355 nm light absorbed is nearly the same in all cases, it is clear that simple parameters such as film thickness, and the related light harvesting efficiency, cannot by themselves account for the observed difference and a specific factor, for example, a favorable active surface-to-volume ratio, plays an important role. A porous surface that allows good electrolyte permeation inside the inner layers of the oxide, a short hole diffusion path, and a good surface free of traps imply more efficient hole scavenging by the electrolyte, which leads to maximizing electron collection. Indeed more effective injection of the holes into the electrolyte results in a larger fraction of collected electrons.

Finally it can be observed that, since we were unable to extract information about chemical capacitance from impedance fitting, we were unable to obtain direct information about the electron lifetime and the relative diffusion parameters under operational conditions.[23] However, the slow photovoltage recovery (seconds) evidenced by laser experiments under open-circuit conditions (Figures S11 and S12 in the Supporting Information) indicates long-lived charge separation and that it should be possible to obtain very high charge collection yields with relatively thick electrodes, as confirmed by the high IPCE values observed in the case of sample 20, if effective electrolyte permeation and related efficient hole transfer to the electrolyte could be assured.

3. Conclusions

The anodization of tungsten in the $NMF/H_2O/NH_4F$ electrolyte has been investigated in detail. The effects induced by anodization time and variable water content in the electrolytic bath on the morphology and on performance were characterized by a combination of structural, steady state, and transient photoelectrochemical techniques. The best composition turned out to be 20% v/v of water and the optimal anodization time was 6 h. A correlation between produced photocurrent, morphology, and charge transport has been evaluated, indicating that vertically oriented, porous, interconnected structures allow efficient interfacial charge separation that was also due to the electric field in the depletion region. Thus, high electron collection efficiencies were observed (60–70%, estimated from IPCE spectra). Due to the observed interconnections, transport across this type of mesoporous film is usually efficient, as testified by photocurrent transients on the millisecond timescale with a sub-millisecond rise time.

The hole transfer process was, as reasonably expected, the critical step for the realization of efficient photoanodes and

care should be taken to develop oxide structures that allow intimate permeation by the electrolyte, enhancing the possibility of successful scavenging of the photoproduced minority carriers, which otherwise undergo recombination processes on the timescale of a few milliseconds. This requirement is particularly important for realizing WO_3 systems with an efficient visible response, since the penetration depth of photons at these wavelengths is sufficiently high to create electron hole pairs along the entire length of a photoactive film a few microns thick.

Experimental Section

Materials

Tungsten foils, *N*-methylformamide, and NH_4F were purchased from Alfa Aesar. Ethanol, acetone, sulfuric acid, and Alconox were purchased from Aldrich. All chemicals were used as received.

Photoelectrode Preparation

Prior to anodization, tungsten laminae about 0.6×2 cm were carefully cleaned with acetone and ethanol and sonicated in an Alconox/water solution to remove surface contaminants and oily or greasy impurities. WO_3 photoanodes were prepared by applying a potential difference of 40 V (Aim-TTi EX752M DC power supply) across the two tungsten laminae, which were kept at a distance of about 3 mm. To avoid electrode corrosion, care was taken to reach the final 40 V in about 1 min. In this way, a passivating compact oxide was formed during the initial stages of anodization. The total duration of anodization ranged from 1 to 7 h in a thermostated bath at 40 °C. These types of electrodes were named 1–7 h after the anodization time employed for their preparation. The electrolyte consisted of NMF to which water 20% v/v and NH_4F 0.05% w/v were added. Another series of samples was prepared by using a variable concentration of water from 10 to 50% v/v, keeping the anodization time fixed at 6 h. The electrodes in this series were named samples 10–50, depending on the percentage of water used in the anodization electrolyte. At the end of anodization the resulting anode, on which an opaque layer of oxide could be clearly observed, was rinsed with water and acetone and cleaned in an ultrasonic bath for 10 min to remove weakly interacting oxide debris (no macroscopic material loss was, however, observed) and fired at 550 °C in air for 1 h to ensure the formation of a nanocrystalline (WO_3 monoclinic) layer.

Structural Characterization

The morphology was characterized by a using scanning electron microscope (FE-SEM Jeol JSM 7600f with an accelerating voltage of 15 kV and SEM Zeiss EVO 40). Cross-sectional WO_3 pictures were taken at tilt angles variable between 70 and 80° after photoablation of part of the WO_3 surface (ca. 0.2 cm^2) by repeated intense ($\approx$140 mJ cm^{-2}) 355 nm laser pulses until the shiny surface of the underlying metallic tungsten was exposed.

The nanoscale morphologies were studied by using tapping-mode AFM (Multimode IIID microscope, Veeco). Surface topography images were taken in air and at room temperature. The surface area was extracted from the AFM images by using Image Metrology SPIP analysis software.

Samples were characterized by XRD by means of a powder diffractometer Panalytical X'Pert Pro using $Cu_{K\alpha}$ radiation ($l=1.5416$ A°), with the X-ray tube set to 40 V and 40 mA. To eliminate contributions from the underlying metal, a special thin-film optical arrangement allowing us to decouple the angle of incidence (ω) from the scattering angle (θ) was employed. Thus, data acquisition was performed under a fixed angle of incidence ($\omega=1$) for 2θ, in the range 5–90° (2θ) with a step size of 0.02° and acquisition time set to 15 s/step.

Photoelectrochemical Measurements

Steady State

J–V curves and EIS (20 mV 5 sin perturbation in the frequency range of 100 000–0.05 Hz) were obtained on an Autolab PGSTAT 30/2 equipped with an FRA2 frequency response analyzer, either GPES or Nova 1.7 (Ecochemie) controlled data acquisition.

Three-electrode configuration measurements were performed by using a Pt wire counter electrode and an SCE reference electrode. In the two-electrode configuration, Pt was used as the counter electrode.

Simulated sunlight irradiation was obtained with an ABET sun simulator equipped with a 150 W Xe lamp and an AM1.5 G filter. A full xenon lamp with a 300 W lamp was also used. The light intensity was calibrated by using a silicon reference cell.

Impedance data were fitted in terms of equivalent circuits by using Zview 3.2c (Scribner Associates). In all cases, a simple circuit of the type shown in Scheme 1 (Randles) satisfactorily fitted the experimental data with relative errors below 5%.

The capacitance was calculated by $C=Y(j\omega)^{n-1}$,[13] in which Y is the CPE admittance and $\omega=2\pi f$, in which f is the frequency corresponding to the maximum of the imaginary part of the impedance; n was also derived by fitting and was in all cases in the range of 0.88–0.97. When $n\approx1$, the CPE element approximates ideal capacitance.

IPCE spectra were obtained by using previously described apparatus[14a–c] under a potential bias of 1 and 1.5 V versus SCE. Since the electrodes were not transparent, the only achievable illumination mode was from the electrolyte side.

Time-Resolved Measurements

Photocurrent transients generated by WO_3 photoanodes, held in a three-electrode configuration (WO_3/Pt/SCE), were collected on an Autolab PGSTAT 30 potentiostat under a potential bias of 1 V versus SCE with a sampling time of 5×10^{-5} s. The frequency-tripled (355 nm) emission of a Q-switched NdYAG laser [full-width at half maximum (FWHM) 7 ns; Continuum Surelite II] served as the excitation source. Laser pulses were attenuated with a benzophenone chemical filter ($T_{355}\approx4\%$) and defocused with a plano-concave lens to achieve pulse energies in the order of (0.15 ± 0.05) mJ/pulse/cm^2. Open-circuit transient photovoltage experiments were carried out in the same experimental setup with an excitation energy of (1.1 ± 0.2) mJ/pulse to achieve a better signal-to-noise ratio.

Acknowledgements

Thanks are due to Roberto Paglino for technical support. P.P.B., V.G.P., and S.G. acknowledge support by projects from Ministerio de Ciencia e Innovación (MICINN) of Spain (Consolider HOPE

CSD2007-00007 and Ramon y Cajal Programme) and Generalitat Valenciana (PROMETEO/2009/058).

Keywords: anodization · hydrogen · laser spectroscopy · photochemistry · tungsten

[1] a) G. K. Mor, O. K. Varghese, M. Paulose, K. Shankar, C. A. Grimes, *Sol. Energy Mater. Sol. Cells* **2006**, *90*, 2011 – 2075; b) K. Shankar, J. I. Basham, N. K. Allam, O. K. Varghese, G. K. Mor, X. Feng, M. Paulose, J. A. Seabold, K. S. Choi, C. A. Grimes, *J. Phys. Chem. C* **2009**, *113*, 6327 – 6359.

[2] A. Kay, I. Cesar, M. Grätzel, *J. Am. Chem. Soc.* **2006**, *128*, 15714 – 15721.

[3] a) C. Santato, M. Odziemkowski, M. Ulmann, J. Augustynski, *J. Am. Chem. Soc.* **2001**, *123*, 10639 – 10649; b) B. D. Alexander, P. J. Kulesza, L. Rutkowska, R. Solarska, J. Augustynski, *J. Mater. Chem*. **2008**, *18*, 2298 – 2303.

[4] M. Higashi, K. Domen, R. Abe, *Energy Environ. Sci.* **2011**, *4*, 4138 – 4147.

[5] a) Z. G. Yi, J. H. Ye, N. Kikugawa, T. Kako, S. X. Ouyang, H. Stuart-Williams, H. Yang, J. Y. Cao, W. J. Luo, Z. S. Li, Y. Liu, R. L. Withers, *Nat. Mater.* **2010**, *9*, 559 – 564; b) Z. Yi, R. L. Withers, Y. Liu, *Electrochem. Commun.* **2011**, *13*, 28 – 30.

[6] H. Zheng, J. Z. Ou, M. S. Strano, R. B. Kaner, A. Mitchell, K. Kalantar-zadeh, *Adv. Funct. Mater.* **2011**, *21*, 2175 – 2196.

[7] J. K. Kim, K. Shin, S. M. Cho, T. W. Leeb, J. H. Park, *Energy Environ. Sci.* **2011**, *4*, 1465 – 1470.

[8] Y. B. Li, Y. Bando, D. Golberg, K. Kurashima, *Chem. Phys. Lett.* **2003**, *367*, 214 – 218.

[9] L. Meda, G. Tozzola, A. Tacca, G. Marra, S. Caramori, V. Cristino, C. A. Bignozzi, *Sol. Energy Mater. Sol. Cells* **2010**, *94*, 788 – 796.

[10] N. R. de Tacconi, C. R. Chenthamarakshan, G. Yogeeswaran, A. Watcharenwong, R. S. de Zoysa, N. A. Basit, K. Rajeshwar, *J. Phys. Chem. B* **2006**, *110*, 25347 – 25355.

[11] a) Y. C. Nah, I. Paramasivam, R. Hahn, N. K. Shrestha, P. Schmuki, *Nanotechnology* **2010**, *21*, 105704; b) W. Lee, D. Kim, K. Lee, P. Roy, P Schmuki, *Electrochim. Acta* **2010**, *56*, 828 – 833.

[12] K. P. Hanke, *Z. Phys. Chemie* **1999**, 212, 1 – 9.

[13] C. S. Hsu, F. Mansfeld, *Corrosion* **2001**, *57*, 747.

[14] a) L. Meda, A. Tacca, C. A. Bignozzi, S. Caramori, V. Cristino, WO 2011/012238, **2011**; b) V. Cristino, S. Caramori, R. Argazzi, L. Meda, G. L. Marra, C. A. Bignozzi, *Langmuir* **2011**, *27*, 7276 – 7284; c) S. Caramori, V. Cristino, L. Meda, A. Tacca, R. Argazzi, C. A. Bignozzi, *Energy Procedia*, unpublished results; d) M. Paulose, K. Shankar, S. Yoriya, E. H. Prakasam, O. K. Varghese, G. K. Mor, T. A. Latempa, A. Fitzgerald, C. A. Grimes, *J. Phys.Chem. B* **2006**, *110*, 16179; e) J. M. Macák, H. Tsuchyia, P. Schmuki, *Angew. Chem.* **2005**, *117*, 2136 – 2139; *Angew. Chem. Int. Ed.* **2005**, *44*, 2100 – 2102.

[15] Y. Guo, X. Quan, N. L. Huimin Zao, S. Chen, *Environ. Sci. Technol.* **2007**, *41*, 4422 – 4427.

[16] Z. Chen, T. F. Jaramillo, T. G. Deutsch, A. Kleiman-Shwarsctein, A. J. Forman, N. Gaillard, R. Garland, K. Takanabe, C. Heske, M. Sunkara, E. W. McFarland, K. Domen, E. L. Miller, J. A. Turner, H. N. Dinh, *J. Mater. Res. J. Mater Res.* **2010**, *25*, 3 – 16.

[17] I. Gaied, S. Dabbous, T. B. Nasrallah, Y. Yacoubi, *J. Phys. Conf. Ser.* **2010**, *214*, 012112.

[18] S. R. Biaggio, R. C. Rocha-Filho, J. R. Vilche, F. E. Varela, L. M. Gassa, *Electrochim. Acta* **1997**, *42*, 1751 – 1758.

[19] J. Bisquert, *PCCP* **2003**, *5*, 5360 – 5364.

[20] F. Di Quarto, A. Di Paola, C. Sunseri, *Electrochimica Acta* **1981**, *26*, 1177 – 1184.

[21] F. Di Quarto, V. O. Aimiuwu, S. Piazza, C. Sunseri, *Electrochimica Acta* **1991**, *36*, 1817 – 1822.

[22] a) S. Kambe, S. Nakade, T. Kitamura, Y. Wada, S. Yanagida, *J. Phys. Chem. B* **2002**, *106*, 2967 – 2972; b) A. Solbrand, H. Lindström, H. Rensmo, A. Hagfeldt, S. E. Lindqvist, S. Södergren, *J. Phys. Chem. B* **1997**, *101*, 2514 – 2518.

[23] J. Bisquert, F. Fabregat Santiago, I. M. Sero, G. G. Belmonte, S. Gimenez, *J. Phys. Chem. C* **2009**, *113*, 17278 – 17290.

Received: January 27, 2012
Revised: March 19, 2012
Published online on April 24, 2012

